Synthetic Jet based Active Flow Control of Dynamic Stall Phenomenon on Wind Turbines Under Yaw Misalignment

Steven A. Tran* and Onkar Sahni†

Rensselaer Polytechnic Institute, Troy, NY, 12180-3590

Dave Corson‡

Altair Engineering, Inc., Clifton Park, NY, 12065

One of the largest contributors to the structural failure of wind turbines is the unsteady aerodynamic loading experienced by the blades. This can arise due to yaw misalignment, wind shear, gusting or a combination of these conditions. Under these conditions, cyclic blade loading occurs and dynamic stall phenomenon is possible which in-turn results in hysteresis and causes vibrations in turbine components. Therefore, it is important to mitigate, or even fully suppress, dynamic stall. In this paper we use numerical simulations to study synthetic-jet based active flow control to mitigate dynamic stall. The goal is to achieve fast-time response control with actuators that require low energy input and are physically compact.

We focus on the NREL Phase VI turbine with the S809 airfoil shape. The baseline configuration (without synthetic jets) is modeled at below rated (7 m/s), rated (10 m/s), and above rated (15 m/s) wind speeds and at a yaw angle of 30°. It is found that the unsteady loading due to yaw misalignment can cause power fluctuations of up to 9kW or 135% for each blade during one blade revolution. Next we study active flow control on a pitching S809 airfoil with a synthetic-jet actuator, where two wind conditions are considered that correspond to the yaw angle of 30°for two wind speeds of 10 and 15 m/s at blade span of 60% and 80%, respectively. The jet is placed at 5% chord location (i.e., x/c = 0.05) and is activated at a non-dimensional frequency of 5. Synthetic-jet based control is shown to significantly reduce the flow separation near the leading edge and thus, reduce the hysteresis by up to 73% at the rated wind speed.

I. Introduction

WIND energy has grown significantly in the past decade and has seen a trend towards the use of wind turbines in more complex conditions. However with this trend comes a need for a greater level of reliability as wind turbine components often fall short of their designed or expected life cycle. This is primarily because of the damage caused to the blades and the gearbox due to the unsteady loading that is experienced under conditions of yaw misalignment, wind shear, gusts, or a combination of these phenomena. These conditions significantly change the local angle of attack and velocity across the span during the course of a blade's revolution. At certain wind conditions, the range of angle of attack experienced by the blade causes the state of the airflow over the blade to oscillate between attached and separated conditions in each revolution leading to cyclic loading. Furthermore, the flow state may be asymmetric with respect to the periodic angle of attack in a revolution cycle, i.e., blade undergoes dynamic stall. This leads to significant variation and hysteresis in the loading of the blade during each revolution, which when experienced regularly, results in structural fatigue and potentially failure of the turbine components.

*Graduate Student, Rensselaer Polytechnic Institute

†Assistant Professor, Rensselaer Polytechnic Institute, AIAA Senior Member

‡AcuSolve Program Manager, 58 Clifton Country Rd., Ste 106, Clifton Park, NY.

Many modern turbine designs address this issue by using various forms of passive and active control techniques.[1,2] One of the most common is active pitch control which alters the pitch of each turbine blade in order to reduce the change in angle of attack and thus, maintain the level of loading on the blade.[3,4] To maximize the extracted power, specifically above cut-off and below-rated wind speeds, the rotor-speed is adjusted based on the generator torque actuator (in variable-speed turbines) to achieve maximum aerodynamic efficiency.[5,6] Similarly, yaw control is applied in order to avoid any misalignment between the rotation axis of the turbine and local wind direction.[1] While these techniques can be effective, altering the pitch, speed, or yaw is relatively slow, energy intensive, and non-local. For example, yaw control may take several turbine revolutions to take effect while uniform blade pitch control may be unable to account for non-local or high-frequency wind events such as those induced by random gusts. Therefore, there is a need for a distributed, efficient, fast-time response method of mitigating, or even fully suppressing, dynamic stall effects (for example, see flow control devices and actuators discussed by Johnson et al[7]).

In this paper we study synthetic-jet based active flow control for wind turbines under yaw misalignment. Synthetic jets are zero-net-mass-flux actuation devices that operate based on the surrounding fluid (from the cross-flow), with alternating ejection and suction of the fluid across an orifice forming a train of vortices.[8] As a form of active flow control, it has been shown to be effective in significantly improving the static stall performance of airfoils. It has been shown that the non-dimensional frequency of actuation, or F^+, has a direct effect on the amount of unsteadiness in the controlled output, where F^+ of 5 or above has been shown to be effective.[9] Moreover, pulse modulation has been shown to further enhance the performance.

Recently, synthetic jets have also been applied to control the unsteady loading on wind turbine blades. For example, the experimental study done by Maldonado et al has demonstrated that synthetic jet actuation was able to almost instantaneously reduce the tip vibrations of turbine blades.[10] Similarly, Taylor et al showed experimentally that unwanted dynamic stall effects on a pitching blade can be reduced using synthetic jets.[11] However, from these studies it has been difficult to obtain details of the flow structures resulting from synthetic-jet actuation and its effect on the overall flow field. In this paper we use numerical simulations to analyze flow fields with and without synthetic-jet actuation and also compute lift-to-drag ratio to demonstrate the feasibility of utilizing synthetic-jet based active flow control for suppressing dynamic stall on wind turbines.

This paper is organized as follows. Section II discusses numerical methodology and Section III presents results. Section IV provides closing remarks.

II. Numerical Methodology

II.A. Flow Solver

In this work, numerical simulations are carried out using a stabilized finite element[12] based flow solver with an implicit generalized-α time integration technique.[13] Due to the low Mach Number flow involved in these cases, incompressible Navier-Stokes equations are used. These are shown in their combined weak form in Equation (1).

$$A(\{\mathbf{w}, q\}, \{\mathbf{u}, p\}) \equiv \int_\Omega [\mathbf{w}\mathcal{L}_m\mathbf{u} + q\mathcal{L}_c\mathbf{u}]\, d\Omega = 0 \tag{1}$$

where $\mathbf{u}$ is the velocity vector, p is the pressure, and $\mathbf{w}$ and q are the weighting functions for velocity and pressure, respectively. These belong to appropriate functions spaces, namely, $\mathbf{u} \in \mathcal{U}$, $\mathbf{w} \in \mathcal{W}$ and p,$q \in \mathcal{P}$ with $\mathcal{U} = \{\mathbf{u} \in H^1(\Omega) | \mathbf{u} = \mathbf{g} \text{ on } \Gamma_g\}$, $\mathcal{W} = \{\mathbf{w} \in H^1(\Omega) | \mathbf{w} = \mathbf{0} \text{ on } \Gamma_g\}$, and $\mathcal{P} = \{p \in L^2(\Omega)\}$, where Ω is the spatial domain, Γ_g corresponds to Dirichlet boundary segment of the domain and $\mathbf{g}$ to specified boundary condition values. $\mathcal{L}_c$ and $\mathcal{L}_m$ correspond to the (strong form) residuals of the continuity (scalar) and momentum (vector) equations, respectively. This is shown below in Equation (2) in indicial notation where Einstein's summation convention is used.

$$\begin{aligned} \mathcal{L}_c\mathbf{u} &= u_{i,i} \\ (\mathcal{L}_m\mathbf{u})_i &= \rho u_{i,t} + \rho u_j u_{i,j} - \rho b_i + \tau_{ij,j} + p_{,i} \end{aligned} \tag{2}$$

Since the Galerkin method for Navier-Stokes equations is known to be numerically unstable, stabilization terms must be added. The method of stabilization used currently is the Galerkin Least Squares (GLS).[12,14] The GLS formulation adds stabilization that allows pressure and velocity to be interpolated at equal orders

and moreover, this is done in a consistent fashion. That is when the exact solution is achieved then the stabilization term has no effect or contribution to the original equations. The semi-discrete stabilized form of the equations are shown in Equation (3).

$$A(\{\mathbf{w}^h, q^h\}, \{\mathbf{u}^h, p^h\}) + \sum_e \int_{\Omega^e} (\mathcal{L}_m^T \mathbf{w}^h) \tau_m (\mathcal{L}_m \mathbf{u}^h)\, d\Omega^e + \sum_e \int_{\Omega^e} (\mathcal{L}_c \mathbf{w}^h) \tau_c (\mathcal{L}_c \mathbf{u}^h)\, d\Omega^e = 0 \tag{3}$$

where Ω^e is the element domain and the superscript T denotes a transpose. Note that τ_c and τ_m are stabilization parameters for the continuity and momentum equations, respectively, definitions of which can be found in Taylor et al.[15] Additionally, the conservation operator has been included in such a way that conservation is maintained.[16]

Since the problems of interest involve flow at high Reynolds number, the unsteady Reynolds-averaged Navier-Stokes (URANS) equations are used instead.[17] This introduces an additional stress term in the momentum equation which corresponds to the turbulent stresses. To close the equations, this additional stress term is modeled with an eddy-viscosity model. The Spalart-Allmaras (SA)[18] one-equation turbulence closure model is used for eddy-viscosity. The SA model is as follows:

$$\begin{aligned}
&\tilde{\nu}_{,t} + \mathbf{u}_i \tilde{\nu}_{i,j} = c_{b1} \tilde{S} \tilde{\nu} - c_{w1} f_w \left[\frac{\tilde{\nu}}{d}\right]^2 + \frac{1}{\sigma}\left(\left[(\nu + \tilde{\nu})\tilde{\nu}_{,i}\right]_{,i} + c_{b2} (\tilde{\nu_{,i}})^2 \right) \\
&\tilde{S} = S + \frac{\tilde{\nu}}{\kappa^2 d^2} f_{v2} \qquad\qquad f_{v2} = 1 - \frac{\chi}{1 + \chi f_{v1}} \\
&g = r + c_{w2}(r^6 - r) \qquad\qquad f_{v1} = \frac{\chi^3}{\chi^3 + c_{v1}^3} \\
&\Omega_{ij} = \frac{1}{2}\left(\frac{\partial u_i}{\partial x_j} - \frac{\partial u_j}{\partial x_i}\right) \qquad\qquad f_w = g\left[\frac{1 + c_{w3}^6}{g^6 + c_{w3}^6}\right]^{\frac{1}{6}} \\
&c_{w1} = \frac{c_{b1}}{\kappa^2} + \frac{1 + c_{b2}}{\sigma} \qquad\qquad \chi = \frac{\tilde{\nu}}{\nu}
\end{aligned} \tag{4}$$

where $\tilde{v}$ is the SA model auxiliary variable, d is the distance from the closest surface (viscous wall), S is a norm of the rate of rotation tensor: $\sqrt{2\Omega_{ij}\Omega_{ij}}$, and the constants are: $c_{b1} = 0.1355$, $c_{b2} = 0.622$, $\kappa = 0.41$, $c_{w2} = 0.3$, $c_{w2} = 2.0$, $c_{w1} = 7.1$, $\sigma = 2/3$. Therefore, the eddy viscosity is defined as:

$$\nu_t = \tilde{\nu} f_{v1} \tag{5}$$

The SA equation can be casted in the form of a scalar advection-diffusion equation, for which we also employ the GLS method[12,?] along with implicit generalized-α time integration.[13]

To summarize, we use the GLS stabilized formulation for the unsteady incompressible Reynolds-averaged Navier-Stokes and Spalart-Allmaras turbulence equations that are discretized by linear finite elements for all solution variables. In order to develop a discrete system of algebraic equations, the weight functions, the solution variables, and their time derivatives, are expanded in terms of the finite element basis functions. Gauss quadrature of the spatial integrals results in a system of first-order, nonlinear differential-algebraic equations. Finally, this system of non-linear ordinary differential equations is discretized in time via the generalized-α time integrator resulting in a non-linear system of algebraic equations. This system is in turn linearized with Newton's method which yields a linear algebraic system of equations that is solved at each time step and the solution is updated for each of the Newton iterations.

To account for blade rotation, a sliding interface technique is employed in the simulations.[19] This is done by defining a rotor disk segment associated with the rotor of the turbine as shown in Figure 1; multiple such segments can be defined for cases with multiple turbines. The mesh in this segment rotates while the surrounding mesh outside of this disk region (i.e., in the outer domain that includes tower and ground/terrain) is kept fixed. This allows the full blade rotation to be incorporated without any mesh distortion, which may occur in cases with highly flexible or deforming structures. The flow solver used is *AcuSolve*™.[20] It is a parallelized code, which uses both message passing interface and threading, and has been shown to scale linearly (in a strong sense) over thousands of processors.

II.B. Full Blade Baseline Setup

For full blade simulations, the NREL Phase VI experimental turbine model is used.[21] This two-blade turbine consists of O(5 meter) blades with the S809 airfoil shape. The setup with the sliding interface for full blade simulations is shown in Figure 1. The blade rotates at a constant rate of 72 RPM. In current simulations both blades are modeled while the tower is not considered.

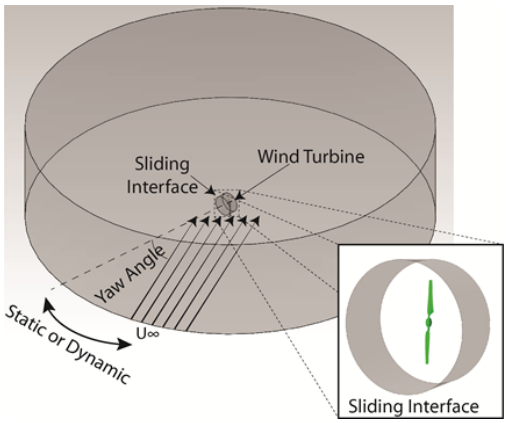

Figure 1: Setup with sliding interface for full blade simulations

About 64 grid points were placed along the chord of the blade and about 75 grid points were used along the majority of the span except near root and tip where the higher grid density was used. Mesh on the blade surface is shown in Figure 2. A boundary layer mesh on the blade was used where the first layer height (in non-dimensional wall units) was such that $y^+ \leq 1$. Mesh refinement regions were used in order to capture flow separation over the suction surface as well as flow structures in the wake. In total, the grid contained roughly 20 million cells. The time-step size used in these simulations was set such that each time-step leads to 1° azimuthal rotation of the blade. Grid and time-step convergence tests were performed for the full blade case where refinement in the grid size and time-step size by a factor of 2 did not show any significant changes in the numerical results. Therefore, the current grid size and time-step size were deemed satisfactory.

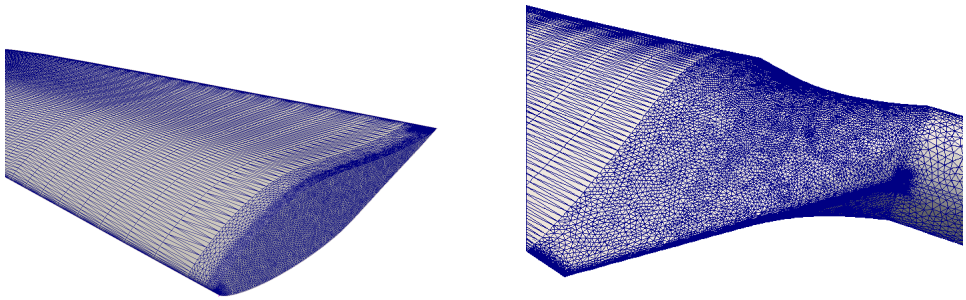

Figure 2: Mesh on blade surface for full-blade baseline case

II.C. Synthetic-jet Setup

The synthetic-jet simulations were carried out on a pitching S809 airfoil. Two wind conditions were considered that correspond to 30°(i.e., high) yaw angle for two wind speeds of 10 and 15 m/s at blade span of 60% and 80%, respectively. The airfoil chord was 0.55 meters and pitched along the quarter chord location. A synthetic-jet actuator was placed at the 5% chord location on the suction side of the airfoil with its orifice oriented along the local normal of the airfoil. The jet neck has dimensions of 1 mm × 5 mm and the cavity has dimensions of 2mm × 8 mm. At the disk or diaphragm location, a velocity profile that is parabolic in space and sinusoidal in time is imposed in order to model the movement of the piezoelectric disk of the synthetic-jet actuator.

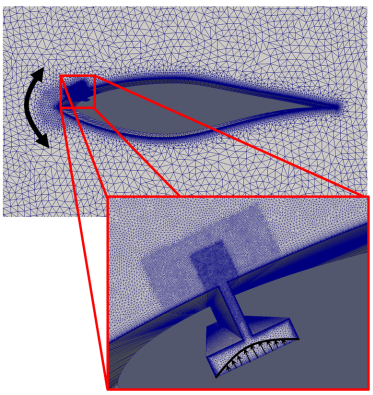

Figure 3: Airfoil and near-jet grid for the pitching S809 airfoil model

The jet actuation depends on the non-dimensional actuation frequency, blowing ratio, and momentum ratio denoted as F^+, C_b, and C_μ, respectively, and are defined as:

$$F^+ = \frac{f_{jet}}{f_{flow}}, \quad C_b = \frac{\langle \overline{V_{neck}} \rangle}{V_\infty}, \quad C_\mu = \frac{\overline{I}_j}{\frac{1}{2}\rho V_\infty^2 A} \tag{6}$$

where f_{jet} is the jet actuation frequency, f_{flow} is the flow frequency related to t_{flight} (time of flight) that is based on the free-stream velocity or wind speed (V_∞) and the chord. V_{neck} is the velocity magnitude at

the jet neck, where the over-bar represents a temporal average and $\langle\cdot\rangle$ represents a spatial average. $\overline{I}_j$ is the time-averaged jet momentum (defined below) and A is the plan-form area of the blade section.

$$\overline{I}_j = \frac{1}{\tau}\rho A_{neck}\int_0^T V_{neck}^2(t)dt \tag{7}$$

where τ is the jet out-stroke time, T is the jet cycle period, ρ is the fluid density in the jet neck, and A_{neck} is the plan-form area of the jet neck.

The grid used in the synthetic-jet cases contained about 128 points along the chord of the airfoil with multiple refinement zones near the jet region to capture the fine-scale jet structures as they exit the jet orifice and advect downstream. The inner most refinement zone contained about 50 grid points along jet orifice. The jet cavity had 256 grid points along the length and 64 along the height. As before, a boundary layer mesh was used where the first layer height was such that $y^+ \leq 1$. In total, the grid contained about 300,000 cells. The grid is shown in Figure 3. The time-step size used for the synthetic jet simulations was such that there were 60 time steps per jet cycle.

III. Results

III.A. Full Blade Baseline Simulations

Full blade simulations were carried out for three wind speeds of 7, 10, and 15 m/s and the yaw angle of 30°. This range of speeds corresponds to the below rated, at rated, and above rated wind speeds of the turbine.

Current numerical predictions are able to accurately capture the pressure distribution along the chord of the blade as compared to the the NREL Phase VI experimental data.[22,23] Figures 4, 5, and 6 show pressure coefficient curves at 80% span and azimuthal positions of 180° and 360° for wind speeds of 7 m/s, 10 m/s, and 15 m/s, respectively. Pressure coefficient is defined as: $C_p = \frac{p-p_\infty}{0.5\times\rho\times V_{ref}^2}$, where p is the local static pressure on the blade's surface, p_∞ is the reference or free-stream static pressure, and denominator is the dynamic pressure based on density and effective reference velocity (V_{ref}). The numerical results are able to capture stagnation point, suction peak pressure and regions with flow separation. Overall, computational results show a good agreement with the experiments.

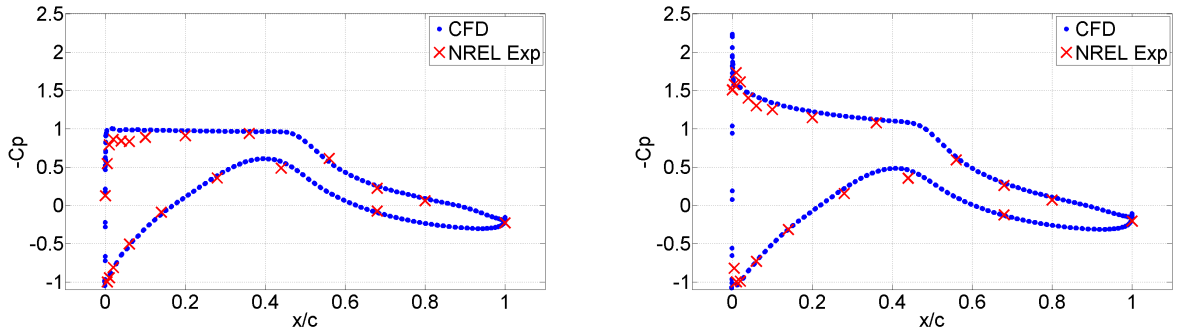

(a) 180°Azimuth (b) 360°Azimuth

Figure 4: C_p for 7 m/s 30° yaw case at the 80% span location at azimuth angles of 180°and 360°

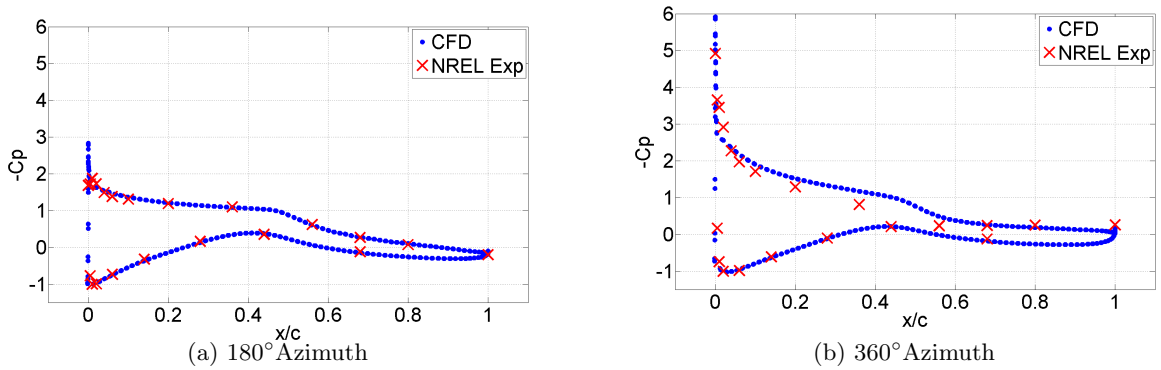

(a) 180°Azimuth (b) 360°Azimuth

Figure 5: C_p for 10 m/s 30° yaw case at the 80% span location at azimuth angles of 180°and 360°

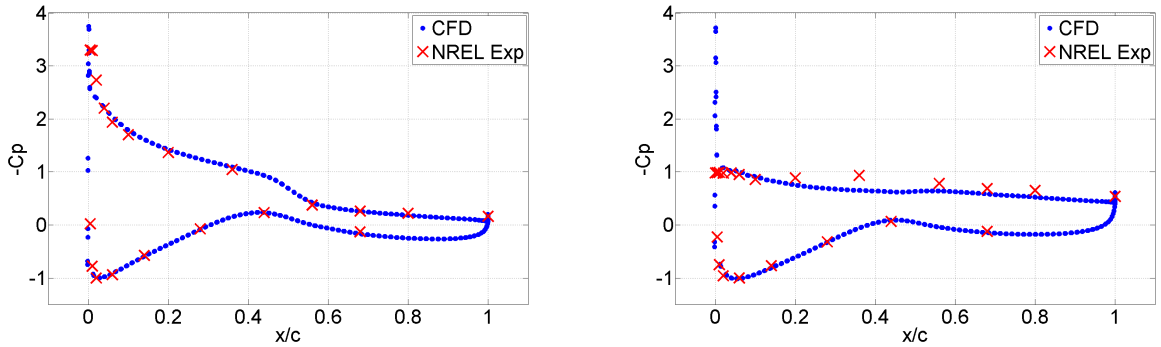

(a) 180°Azimuth (b) 360°Azimuth

Figure 6: C_p for 15 m/s 30° yaw case at the 80% span location at azimuth angles of 180°and 360°

At 7 m/s, the effective angle of attack observed by the turbine blade is low so the flow is predominately attached throughout the turbine revolution, even when severe yaw misalignment is present (i.e., 30° yaw). Marginal oscillations of about 2.5% in the total power are observed in the 7 m/s 30° yaw case. At higher wind speeds of 10 m/s and 15 m/s, the unsteadiness in the flow over the airfoil due to yaw misalignment increases significantly. The oscillations in the total power increase to 7.6% and 12.3% for the 10 m/s 30° yaw case and the 15 m/s 30° yaw case, respectively. This can be observed in Figure 7. This increase in power oscillations occurs because the range of angle of attack experienced along the span of the blade increases significantly, especially at higher wind speeds. Thus, significant portions of the blade begin to experience unsteady, periodic effects such as dynamic stall at higher wind speed. Therefore, in the rest of this study only wind speeds of 10 m/s and 15 m/s will be discussed.

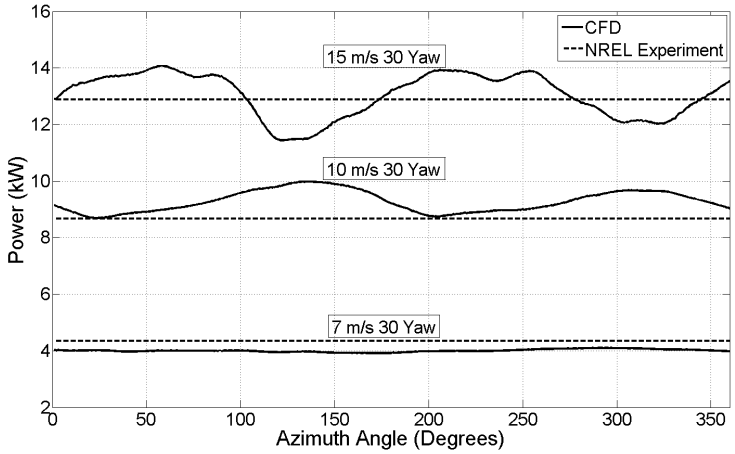

Figure 7: Overall power generated by the rotor at 7, 10, and 15 m/s with 30° yaw

Because the NREL rotor is comprised of two blades, the blades are 180° out of phase with each other. In turn, the oscillations in the total power cancels out majority of fluctuations experienced by individual blades. Therefore in order to see the full extent of the unsteadiness, one must look at each blade individually. This is straightforward to obtain in simulations. Figures 8 and 9 show power due to each blade for 10 m/s and 15 m/s cases at 30°yaw, respectively. At a wind speed of 10 m/s and 30° yaw, the power generated by a single blade can fluctuate by as much as 1.5 kW or 35% in one revolution. At 15 m/s and 30° yaw, the power generated fluctuates by as much as 9 kW or 135% in a revolution, where the flow is found to be separated for most portions of the revolution cycle and over much of the blade except near the tip where the angle of attack is relatively low and tip vortex further reduces the induced angle of attack. Under these conditions, most of the blade experiences dynamic stall which results in significant unsteady loading on the turbine components.

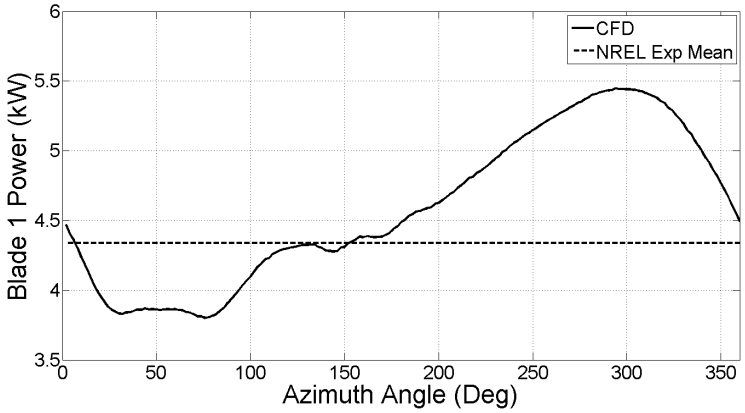

Figure 8: Power due to single blade at 10 m/s with 30° yaw

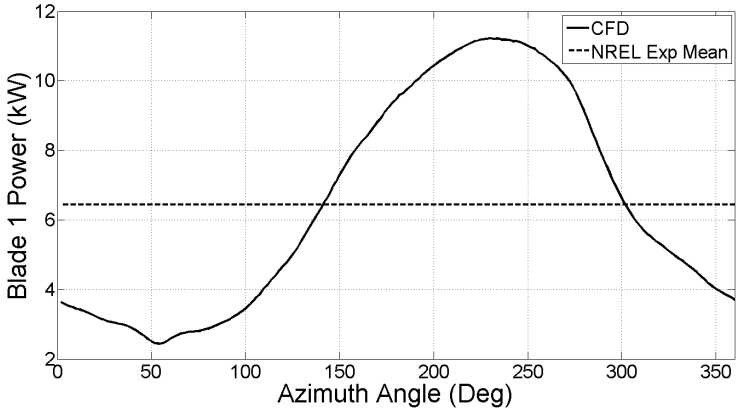

Figure 9: Power due to single blade at 15 m/s with 30° yaw

III.B. Synthetic-jet Simulations

Two cases have been studied using the dynamic pitching airfoil model. Each of these cases were selected to model the flow that is experienced by a section of the full blade under certain wind conditions. The changes in angle of attack due to yaw for a certain blade section were calculated analytically and imposed on the dynamic pitching model. The two cases that were considered include 10 m/s 30° yaw at 60% blade span and 15 m/s 30° yaw at 80% blade span. These were selected in order to cover the broad range of conditions experienced along the span of the blade at different wind speeds and yaw angles. The outboard portion is focused on as it has a major contribution to the power. The resulting non-dimensional parameters such as the reduced pitching frequency (k) and the average Reynolds number based on the chord ($\overline{Re_c}$) are listed in Table 1.

Table 1: Parameters for the 2D dynamic pitching model

Case	Wind Speed	Yaw Angle	% Span	$\overline{Re_c}$	α	k	F^+	C_b	C_μ
I	10 m/s	30°	60	9.35e5	15.5°± 4.25°	0.0839	5	0.875	0.0028
II	15 m/s	30°	80	1.00e6	20.0°± 5.50°	0.0755	5	0.875	0.0026

For the 10 m/s 30° yaw 60% span case, the flow seems to stall at the upper end of the pitching cycle at 19.75° angle of attack and reattaches during the downstroke at approximately 14°. On the other hand, for the 15 m/s 30° yaw 80% span case, the flow remains attached until approximately 21° angle of attack on the upstroke, where the flow separates at the leading edge, while the flow remains completely separated for the entirety of the downstroke and does not reattach until the upstroke begins again. The flow stalls at the leading edge of the airfoil for both cases. The dynamic stall in these two cases results in significant amount of undesirable unsteadiness in the lift and drag. This is evident in the hysteresis loops, see Figures 12 and 13.

To reduce this unsteadiness, synthetic-jet actuation is applied to these two cases. In order to mitigate dynamic stall, it is necessary to place the jets close to the prominent flow separation location. Therefore in these cases, the jet was placed at the 5% chord location. Jets were actuated at F^+ of 5 and C_b of 0.875. It has been shown that actuation frequencies of this order are effective for controlling stall. This results in a momentum coefficient of about $C_\mu = 0.3\%$ for both cases. When the synthetic jet actuation is activated, the effect of the control on the flow becomes apparent within the first pitch cycle.

Synthetic jet actuation perturbs the flow near the leading edge in such a way that it forces the flow in this region to reattach sooner than it would in the baseline case (without synthetic-jet actuation). Earlier flow reattachment significantly reduces the severity of dynamic stall that is otherwise observed in most portions of the pitch cycle. This in-turn results in a lower pressure drag as well as more lift generation. For the 10 m/s 30° yaw 60% span case with synthetic jet actuation, the flow reattaches during the downstroke at approximately 16° angle of attack as opposed to 14° angle of attack as seen in the baseline case. The maximum lift is decreased due to jet activation in the upstroke, however, lift is increased during the downstroke. This results in an overall reduction in unsteadiness in the lift. Drag is reduced significantly throughout the entire pitch cycle for this case due to the reduced flow separation.

For the 15 m/s 30° yaw 80% span case, the flow begins to reattach at approximately 18° angle of attack with actuation as opposed to 14.5° angle of attack during the downstroke. Because of the flow separation reduction provided by the synthetic-jet actuation at the leading edge, more lift is generated throughout the entire pitch cycle. Drag reduction is seen at the lower range of angles of attack experienced for this case. For both cases, the jets seem to lose effectiveness at very high angles of attack (i.e., over 20°angles of attack) due to the strong adverse pressure gradients and massively separated flow. Overall, synthetic-jet actuation results in a 73% and 62% reduction in the L/D ratio hysteresis for the two cases of 10 m/s and 15 m/s, respectively.

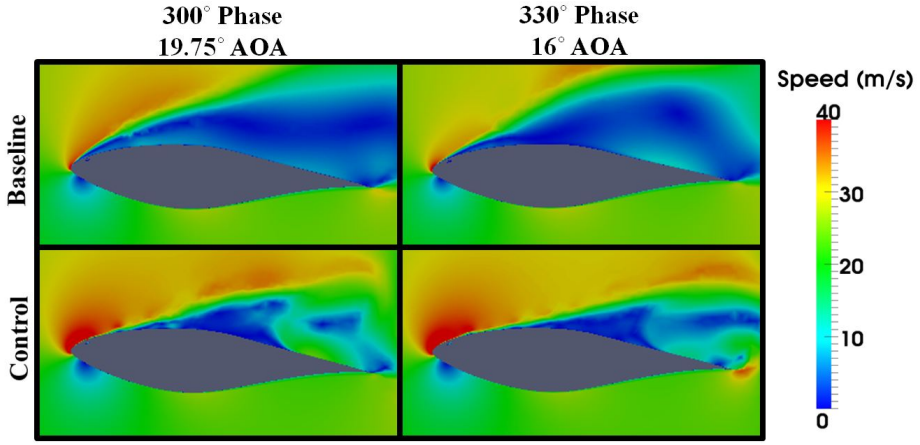

Figure 10: Flow speed contours with (control) and without (baseline) actuation for 10 m/s 30° yaw 60% span case

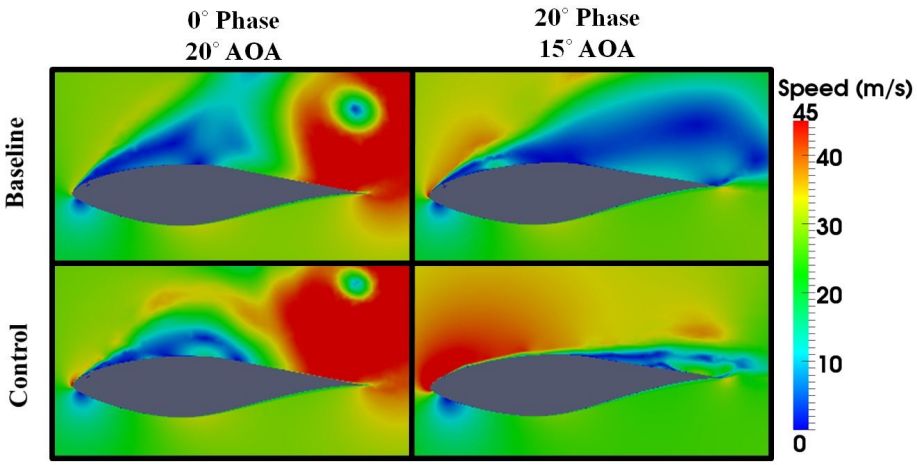

Figure 11: Flow speed contours with (control) and without (baseline) actuation for 15 m/s 30° yaw 80% span case

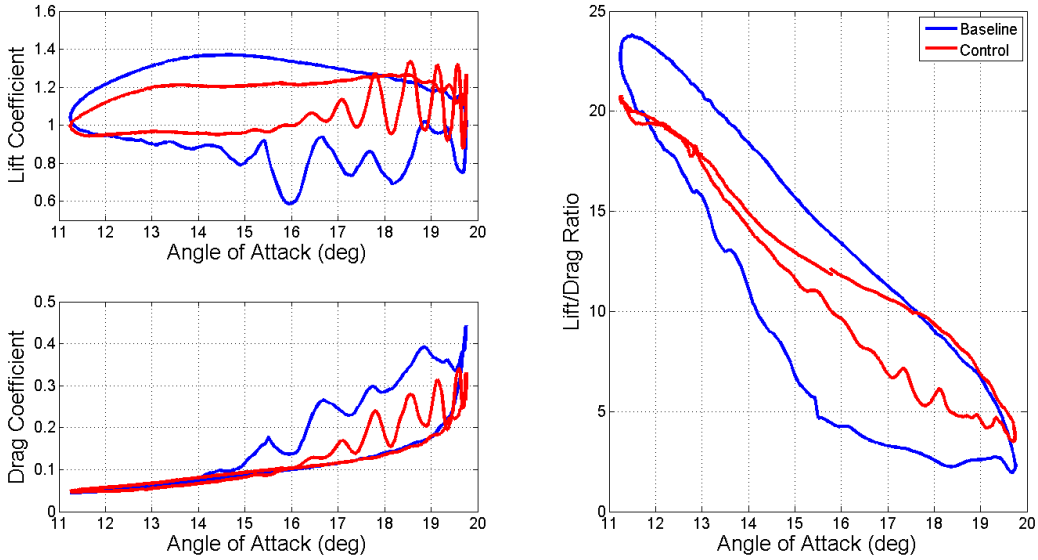

Figure 12: Coefficients of lift and drag, and L/D ratio with (control) and without (baseline) actuation for 10 m/s 30° yaw 60% span case

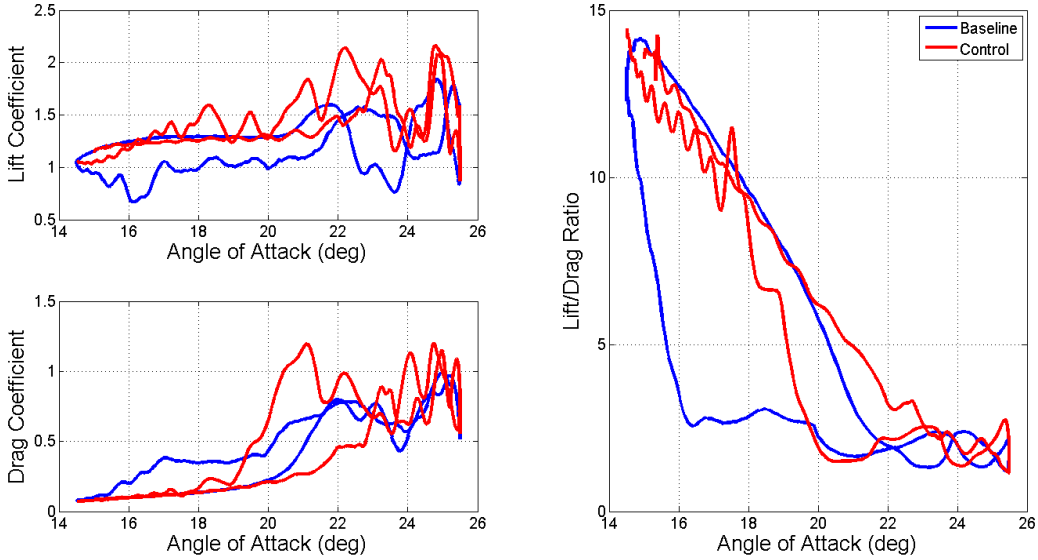

Figure 13: Coefficients of lift and drag, and L/D ratio with (control) and without (baseline) actuation for 15 m/s 30° yaw 80% span case

IV. Closing Remarks

Numerical simulations were carried out to investigate the effects of active flow control on mitigating dynamic stall phenomenon, which can arise due to yaw misalignment of wind turbines. First, the baseline configuration of the NREL Phase VI blade was considered under different wind conditions that correspond to above, at, and below rated speeds (i.e., 7 m/s, 10 m/s and 15 m/s) and 30° yaw misalignment. These simulations showed that with yaw misalignment, during each blade revolution the blade loading may fluctuate by as much as 35% at rated speed and by as much as 135% at above rated speed. Numerical results for the full-blade baseline configuration showed good agreement with experiments. Next we studied active flow control on a pitching S809 airfoil with a synthetic-jet actuator, where two wind conditions are considered that correspond to a 30° yaw misalignment for two wind speeds of 10 and 15 m/s at blade span of 60% and 80%, respectively. Synthetic jets were placed at the 5% chordwise location and normal to the airfoil surface. Jets were actuated at a non-dimensional frequency of 5 relative to the flow time-of-flight. Synthetic jet actuation was shown to significantly reduce flow separation and therefore was able to reduce the hysteresis (in the lift-to-drag curves) by as much as 73%.

Acknowledgments

This work has been supported by a NYSERDA grant monitored by Dr. Barry Liebowitz as well as a research grant under NASA's New York Space Grant program. *AcuSolve*™ software provided by Altair Engineering Inc. was used for flow simulations and *MeshSim* software provided by Simmetrix Inc. was used for mesh generation. Computational resources provided by the Center for Computational Innovations (CCI) at Rensselaer were used. Experimental data was provided by Dr. Scott Schreck and the National Renewable Energy Laboratory. Adam Fisher (undergraduate student) assisted greatly in this work for running and processing simulations.

References

[1]Burton, T., Sharpe, D., Jenkins, N., and Bossanyi, E., *Wind Energy Handbook*, 2001.

[2]Pao, L. and Johnson, K., "Control of Wind Turbines: Approaches, Challenges, and Recent Developments," *IEEE Control Systems Magazine*, 2011, pp. 44–62.

[3]Geyler, M. and Caselitz, P., "Robust multivariable pitch control design for load reduction on large wind turbines," *J.*

Solar Energy Eng., Vol. 130, No. 3, 2008, pp. 1–12.

[4]Laks, H., Pao, L., Wright, A., Kelley, N., and Jonkman, B., "Blade pitch control with preview wind measurements," *Proc. AIAA/ASME Wind Energy Symp.*, AIAA, Orlando, Florida, 2010.

[5]Freeman, J. and Balas, M., "An investigation of variable speed horizontal- axis wind turbines using direct model-reference adaptive control," *Proc. AIAA/ASME Wind Energy Symp.*, AIAA, Reno, Nevada, 1999.

[6]Song, Y., Dhinakaran, B., and Bao, X., "Variable speed control of wind turbines using nonlinear and adaptive algorithms," *J. Wind Eng. Ind. Aerodyn.*, Vol. 85, 2000, pp. 293–308.

[7]Johnson, S., van Dam, C., and Berg, D., "Active Load Control Techniques for Wind Turbines," Sandia national lab, Aug. 2008.

[8]Glezer, A. and Amitay, M., "Synthetic Jets," *Annual Review of Fluid Mechanics*, Vol. 34, No. 1, 2002, pp. 503–529.

[9]Glezer, A., Amitay, M., and Honohan, A. M., "Aspects of low-and high-frequency actuation for aerodynamic flow control," *AIAA journal*, Vol. 43, No. 7, 2005, pp. 1501–1511.

[10]Maldonado, V., Farnsworth, J., Gressick, W., and Amitay, M., "Active control of flow separation and structural vibrations of wind turbine blades," *Wind Energy*, Vol. 13, No. 2, 2010, pp. 221–237.

[11]Taylor, K., Leong, C. M., and Amitay, M., "Dynamic Load Control on a Finite Span Wind Turbine Blade Using Synthetic Jets," *Proc. 50th AIAA Aerospace Scienced Meeting including the New Horizons Forum and Aerospace Exposition*, AIAA, Nashville, Tennessee, 2012, pp. 6–9.

[12]Hughes, T., Franca, L., and Hulbert, G., "A new finite element formulation for computational fluid dynamics: VIII The Galerkin/least squares method for advective-diffusive equations," *Comp. Methods Appl. mech. Eng.*, Vol. 73, No. 2, 1989, pp. 173–189.

[13]Jansen, K. E., Whiting, C. H., and Hulbert, G. M., "A generalized-α method for integrating the filtered Navier-Stokes equations with a stabilized finite element method," *Computer Methods in Applied Mechanics and Engineering*, Vol. 190, No. 3, 1999, pp. 305–320.

[14]Johnson, K. and Bittorf, K., "Validating the Galerkin Least-Squares Finite Element Methods in Predictng Mixing Flows in Stirred Tank Reactors," *Proceedigns of CFD*, 2002.

[15]Taylor, C., Hughes, T., and Zarins, C., "Finite element modelling of blood flow in arteries," *Comput. Methods Appl. Mech. Engr.*, Vol. 158, 1998, pp. 155–196.

[16]Hughes, T. and Wells, G., "Conservation properties for the Galerkin and stabilised forms of the advection.diffusion and incompressible Navier.Stokes equations," *Computer Methods in Applied Mechanics and Engineering*, Vol. 194, No. 9-11, 2005, pp. 1141–1159.

[17]Wilcox, D. C., *Turbulence Modeling for CFD*, D C W Industries, 2006.

[18]Spalart, P. R. and Allmaras, S. R., "A one equation turbulence model for aerodynamic flows," *AIAA*, Vol. 94, 1992.

[19]Corson, D. A., Griffith, D. T., Ashwill, T., and Shakib, F., "Investigating Aeroelastic Performance of Multi-MegaWatt Wind Turbine Rotors Using CFD," *Proc. 53rd AIAA/ASME/ASCE/AHS/ASC Structures, Structural Dynamics and Materials Conference*, AIAA, Honolulu, Hawaii, 2012.

[20]"Computational Fluid Dynamics (CFD) flow solver," http://www.altairhyperworks.it/Product,54,AcuSolve.aspx, Accessed: 2013-12-11.

[21]Hand, M. M., Simms, D., Fingersh, L., Jager, D., and Cotrell, J., "Unsteady Aerodynamics Experiment Phase VI: Wind Tunnel Test Configurations and Available Data Campaigns," Tech. rep., Dec. 2001.

[22]Schreck, S., personal communication, 2012.

[23]Simms, D. A., Schreck, S., Hand, M., and Fingersh, L., *NREL unsteady aerodynamics experiment in the NASA-Ames wind tunnel: A comparison of predictions to measurements*, National Renewable Energy Laboratory Colorado, USA, 2001.